Dynamical equilibrium of avalanches on a rough plane

Adrian Daerr[a)]

Laboratoire de Physique Statistique de l'ENS, 24 rue Lhomond, 75231 Paris Cedex 05, France[b)]

We present experimental results on avalanches which are triggered in a metastable static layer on a rough inclined plane. We observe that despite the continuous increase in mass of a perturbation while it runs down, the flow reaches a dynamical equilibrium where the fronts evolve at constant speed and the mass is spread. The head front is found to be a shock wave with a crest, and its transient acceleration phase is studied. In contrast, the rear front grows in a self-similar manner from the beginning. An instability is observed which breaks thin flowing layers down into solitary waves. © *2001 American Institute of Physics.* [DOI: 10.1063/1.1377864]

I. INTRODUCTION

At regular intervals and throughout the world, avalanches of snow, rock debris, or volcano ashes provoke great damage because they are difficult to predict. Next to the problem of foreseeing an avalanche or a landslide, a major unknown is the actual size and evolution of such an event. This is due to the fact that on one hand we know little about the dynamics of the materials involved, and on the other that the mass of a flow of solid particles can evolve along its trajectory. The flow can incorporate underlying material on its way down, but also deposit partially on shallow slopes. This is most spectacular in snow avalanches, whose potential to amplify from a snow ball has given the word ''avalanche'' its figurative meaning.

The numerous studies on free-surface flows of particulate materials[1–7] focus on the rheological aspect, studying the flow of an entirely mobilized quantity of matter on different solid surfaces. In contrast, the experiment presented here considers the flow down a plane already covered by a static layer of the same material that is flowing. The flow can therefore change its mass by setting this material into motion. This changes the dynamics of the flow: An increase in momentum can be achieved by an increase of the moving mass instead of by accelerating.[8]

The experiments are done with dry glass beads. The materials involved in avalanche, debris, or pyroclastic flows are much more complex, and unique to the geographic location in which they occur (type of material, size distribution of solid particles, etc.), and on the history (weathering, aging, rainfalls, etc.). Very often however, they are modeled as a dry granular material, because this simplifies the description while capturing some key features of the complex natural mixtures.

The most prominent among these is the existence of a threshold stress for motion to occur in granular material: Sand can have a nonhorizontal surface, up to a critical static angle φ_s, at rest. When this is exceeded, the sand starts

flowing, and will not stop before the surface slope has decreased below a second threshold, the dynamical angle $\varphi_d < \varphi_s$. There is therefore a hysteresis between the dynamical and static states.[9] Between the two critical angles, the static system is metastable, and will start flowing if perturbed. This is the principle of the experiment presented here.

We will study the evolution of the resulting avalanches. We ask questions that arise also in practical situations concerned with avalanches: how will the initial perturbation evolve in mass, extension? Will it amplify indefinitely, and if so at what rate? Are there quantities that saturate, among mass, velocity, height, lateral, or longitudinal extension? How is the material distributed along the avalanche? Is there a simple relation between overall mass, height, and speed?

In Sec. II, we will present the experimental apparatus and measurement techniques. Section III deals with the particular regime of nonamplified flows, where the flow does not gain any mass on average. Then (in Sec. IV) amplifying flows or avalanches are investigated, and Sec. V concludes on our results.

II. EXPERIMENTAL SETUP

The experiments are done on an inclined plane covered with velvet cloth (Fig. 1). This surface is chosen so that the glass beads (180–300 μm in diameter), our granular material, have a larger friction with it than between themselves. A thin layer of grains can thus remain static on the plane up to a larger angle than if it were on a grain pile. We set the plane to an angle φ (larger than the pile angle $\varphi_d \simeq 24°$) and pour glass beads abundantly at the top. The moving beads leave behind a static layer of uniform thickness $h(\varphi)$ (arrow leading to point a in Fig. 2). This effect is explained by the variation of the friction of the successive grain layers with their distance to the surface of the inclined slope:[10] It is maximum for the bottom layer, and decreases continuously to the value for a thick pile. The top static layer is that which has a large enough friction coefficient $\mu(h)$ on the underlying layers to come to a stop. At inclination angle φ, the friction coefficient of this top static layer is then $\mu(h)$
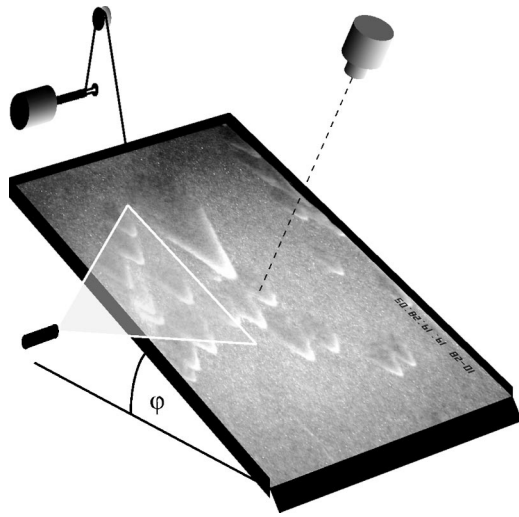
FIG. 1. Experimental setup. The plane is 1.35 m long and 0.62 m large, and its rough surface is velvet cloth. The tilt angle is adjusted by means of a winch operated by a synchronous motor at $1°$/min. A camera is fixed to the plane at about 2 m above it. We measure the height of the flow with a light sheet, which hits the layer at a small angle of incidence. The lateral displacement of the intersection line, as seen by the camera, is proportional to the layer thickness.

$=\tan \varphi$. The measurements $h(\varphi)$ of Fig. 2 thus give the variation of the coefficient of friction with depth.[7] We obtain a simple exponential decay as in Ref. 7:

$$\mu(h) = \mu(\infty) + \Delta \mu \exp(-h/h_0) \qquad (1)$$

with h_0 of the order of $2d$, where $d = 240\,\mu$m is taken as the mean diameter of the grains, and $\Delta \mu = \mu(0) - \mu(\infty)$ is the difference between the friction coefficient at the plane and that in the pile.
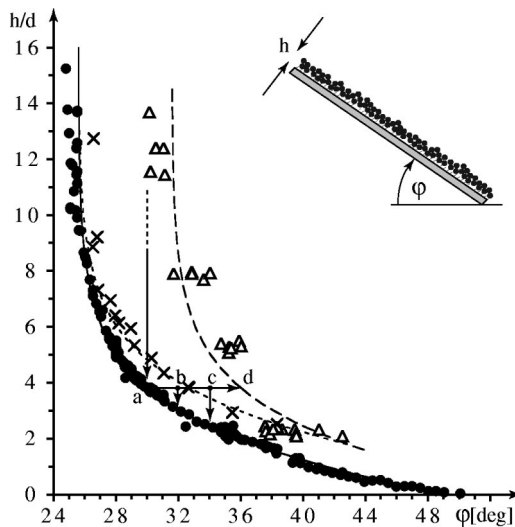

FIG. 2. Stability diagram. Main graph: The solid line and circles give the dynamical height, at which a moving layer freezes (arrow leading to point a). A static layer of given height can be tilted up to the static angle before becoming unstable (long-dashed line and open triangles, arrow leading to point d). The metastable region in between is divided by the dotted line and crosses into a domain where triangular avalanches are observed (e.g., triggering at point b) and another where avalanches propagate uphill (e.g., point d). Inset: Notations.
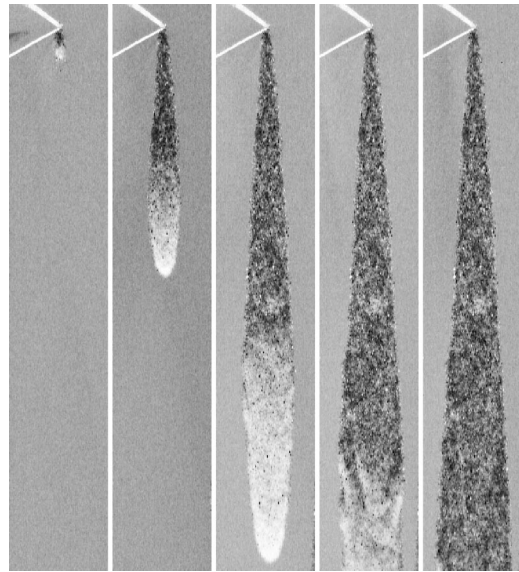

FIG. 3. Evolution of a triangular avalanche. An image of the unperturbed plane has been subtracted, so that the regions without change appear as uniform gray, the excess height of the avalanche brighter and the shallower tracks darker. The preparation angle is $\varphi = 30°$, and the additional tilt is $\delta\varphi = 1°$. The avalanche was triggered with a pointed object which is visible (with its shadow) at the origin. The time lapse between consecutive images is 3.24 s, and the image is 81 cm high.

The layer which is obtained in this way is dynamically stable: If we set the grains in motion by giving the experiment a jolt, they stop again in a fraction of a second. The corresponding angle is called the dynamical angle $\varphi_d(h)$, and is just given by inverting the relation $h(\varphi)$ measured in Fig. 2. The layer can be tilted up to a second critical angle, called the statical angle $\varphi_s(h)$, where it starts moving spontaneously (point d in Fig. 2). The measurements of this angle show much more scatter, but show a similar increase for thin layers. We have supposed when drawing the long-dashed line in Fig. 2 that, following Pouliquen,[10] it is at a constant distance ($6°$ as in Ref. 10) from the dynamical angle. The greater scatter is possibly due to the fact that while the stopping dynamical angle involves all mobile particle and consequently averages over their properties, the static angle depends on the instability of individual surface grains.[11]

Between the dynamical angle φ_d and the static angle φ_s the layer is metastable, and a perturbation triggers an avalanche which grows as it goes down. As was reported in Ref. 11, the perturbation threshold for setting off an avalanche behaves in a way characteristic of a subcritical bifurcation: It is greatest at the dynamical angle $\varphi_d(h)$, and decreases to zero as the angle is increased. Within the hysteresis, two different shapes of avalanches exist: For angles close to the preparation angle φ, the avalanche grows laterally, leaving a triangular track where the layer thickness has decreased to the new dynamical height $h(\varphi + \delta\varphi)$ (Fig. 3). For greater additional tilt $\delta\varphi$ to the preparation angle, the instability also propagates uphill, that is the layer uphill from the origin becomes unstable and starts flowing itself (Fig. 4).

Part of the plane is filmed (at 50 Hz) by a charge coupled device camera, located at about 2 m from the plane with its optical axis perpendicular to it. To measure the height of the
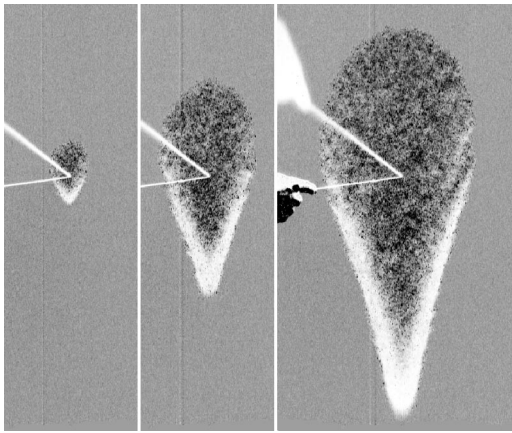
FIG. 4. Evolution of an uphill propagating avalanche. The layer was prepared at $\varphi = 30°$ as in Fig. 3, but the additional tilt is now $\delta\varphi = 4°$. The grains of course still move downwards, but an instability front now propagates in the opposite direction and mobilizes the static layer uphill from the origin. The stick used to trigger the avalanche is pointing at its origin. The time lapse between consecutive images is 0.84 s, and the image is 87 cm high.
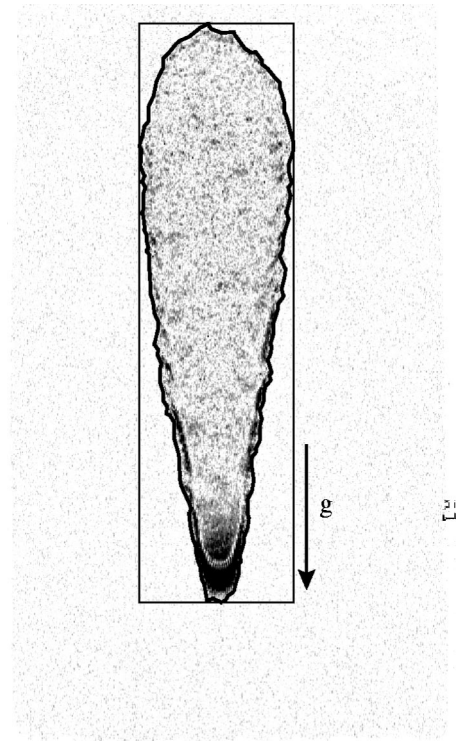

FIG. 5. Measurements performed on avalanches. This example shows an uphill-propagating avalanche as image difference. The up-, down-, left-, and rightmost points are obtained by circumscribing a rectangle. For detailed analysis of the avalanche shape, the outline is detected using a program that finds a hull enclosing the dark dots which characterize motion.

granular layer, we direct a sheet of light at the plane at a small angle of incidence ($<10°$). The intersection of this light sheet with the layer creates a bright line of diffused light. The position of this line, as seen by the camera, depends strongly on the local thickness of the layer. Using a calibration setup, we can calculate the height of a point on the line. We achieve subpixel precision in the line position by fitting a Gaussian intensity distribution to its cross section, and obtain an overall precision on the height of $20\,\mu$m or better (depending on the value of the camera zoom). It might seem superfluous at first to aim at such precision when the mean grain diameter is $240\,\mu$m; but the light beam is much larger than a single grain (the intersection line is roughly $10d$ large), averaging over their heights, and it turns out that this average is a well-defined quantity which shows continuous variations down to fractions of a bead diameter (Fig. 2).

On the difference of successive images, the moving part of the avalanche can be clearly made out (see Fig. 5). This is because the not perfectly spherical beads reflect and focus some light rays into the camera in certain orientations. The layer, instead of appearing as continuous white (we do not resolve the beads individually), is therefore studded with bright spots from beads which by chance have the right orientation to reflect light into the camera, and motion is easily recognizable (to the human eye) as a scintillating domain where bright spots appear and disappear from one video-frame to the next. This results in an image difference where the regions which have changed appear as point clouds.

Two types of measurements were done on these image differences (see Fig. 5): To measure the propagation velocities, a rectangle with sides parallel, respectively, perpendicular to the direction of steepest slope was circumscribed to the moving part to find its left-, right-, bottom-, and topmost points, whose positions were then plotted as a function of time. To study the shape of the fronts in detail, we implemented a program to find the whole boundary of the ava-

lanche as a function of time. For every image, the program starts with a small contour somewhere inside the moving domain, and extends it progressively to any point it finds within a certain distance outside the existing contour.

III. FLOW WITHOUT AMPLIFICATION

On a uniform, dynamically stable layer (created at an angle φ as described previously), we create a straight front of moving material, by pushing the granular matter at the top with a bar on all the width of the plane. The distance and speed of this bulldozing (done by hand) determine the mass and initial speed of a moving quantity granular matter that runs down the plane (Fig. 6). Because the inclination was not changed after the preparation, the layer thickness left behind this moving stripe is the same as in front of it. The mean moving mass is therefore conserved.

There is however a noticeable mass exchange between the layer and the moving part, as can be seen by using tracer particles. We observe that the surface velocity of the grains at the head front equals the velocity of the front. But this surface velocity decreases quickly behind the front. A tracer particle is thus lifted up by the head front, moves with it, but eventually reduces its speed, falls back, and settles to rest at the rear front. The wave is therefore not a material wave: As time proceeds, the grains contained in the wave are progressively replaced by newly mobilized ones as the former are evacuated to the back. This wave is thus mostly a wave of mobilization/deposition.
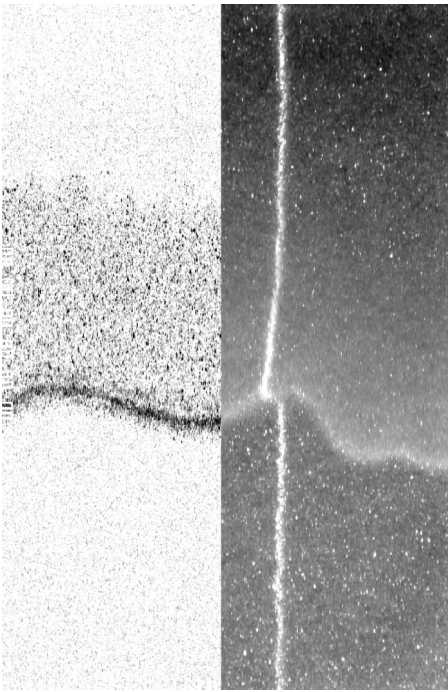
FIG. 6. Isolated front. At the preparation angle, an excess strip of matter moves down without amplifying. The layer is immobile in front of and behind it (the left half shows an image difference between two images 0.02 s apart). A light sheet at small incidence allows for height measurements (bright line in the right half). It can be seen that the thickness of the layer is unchanged by the stripe. As it moves downwards, the front becomes undulated.

The front does not remain perfectly straight, but becomes undulated with time (Fig. 6). This is not a self-amplifying instability like, for instance, the fingering observed by Pouliquen,[12] as the differences increase linearly in time. It is rather the effect of inhomogeneities in the layer thickness, which lead to small fluctuations of the speed of the moving front (as will be seen in the following).

The first result, as shown in Fig. 7, is that at any angle, the height of a moving mass of granular matter on the plane is limited to a small interval of possible values. If too small fronts are created, they will eventually stop (see Fig. 8). First the front becomes irregular due to velocity fluctuations, and then the slowest parts (which are the thinnest) stop and the front breaks into separated packets. This again exhibits the subcritical nature of the transition between static and mobile states in granular matter: If the momentum of a moving mass becomes too small, it gets trapped into the static state. Now each remaining packet has lateral boundaries and looses matter by depositing static ridges, until the size of the packet becomes so small that it freezes completely (see Fig. 8). A very big initial strip, on the other hand, spreads in the direction of motion, reducing its height. Then it becomes unstable (see Fig. 9) and breaks up into several smaller strips which follow one another.

Only for a certain intermediate size, the stripe propagates unperturbed as a solitary wave. It is characterized by a steep head front (shock) and a monotonic decrease of the height toward the back. Considering that before and after it the grains are motionless, we call it a lonely wave. Its relative moving height, defined as maximal height with respect
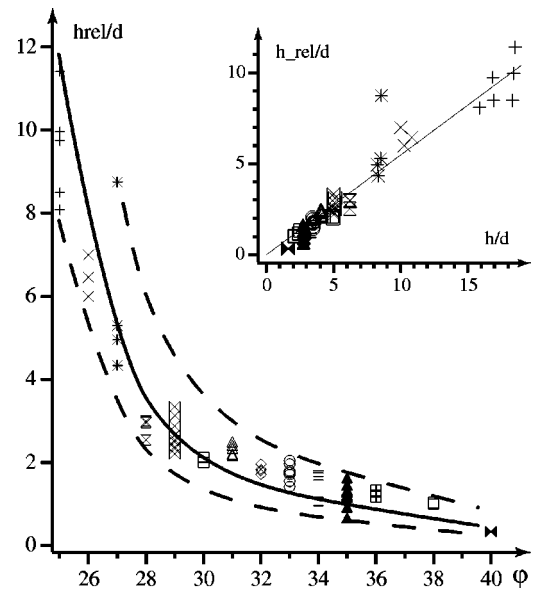

FIG. 7. Height of a moving stripe. Main graph: Relative height of a stripe (height with respect to the static layer thickness h_d), as a function of the plane inclination φ. At any angle, the range of accessible heights is limited (see also Fig. 9). Inset: Relative height as a function of the static layer thickness h_d. The solid line is the best-fit ratio 0.55. Heights are expressed in mean grain diameters ($d=240\ \mu$m) and the symbols identify the measurements at different angles.

to the height of the static layer in front ($h_{rel}=h_{crest}-h_d$), is proportional to the thickness of the static layer (inset of Fig. 7), $h_{rel}\simeq(0.55\pm0.1)h_d$.

The second result is that the velocity decreases with increasing slope of the plane, but does not drop below a minimum velocity which is close to the dimensional velocity $\sqrt{gd}$ (Fig. 10). This velocity is roughly the one acquired by one grain after a free fall over the distance d, and gives a naïve estimation of the velocity of a single grain on a rough inclined surface.[13,14] That this velocity is measured corresponds to the fact that for high inclination angles the relative moving height becomes of the order of one grain diameter precisely (see the inset of Fig. 10).
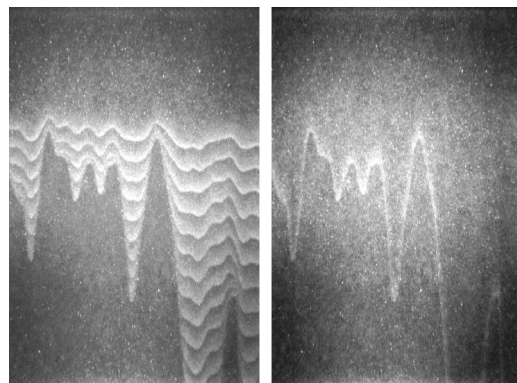

FIG. 8. Stopping of a small front and creation of ridges. Left: Superposition of images 0.64 s apart. The front first stops where it is concave. The remaining drops then lose material on the sides and shrink until they freeze as well, forming triangles pointing downwards. The deceleration phase is very short, the velocity changes only just before the trapping. Right: Image at the end of the flow. The stopping material has created ridges.
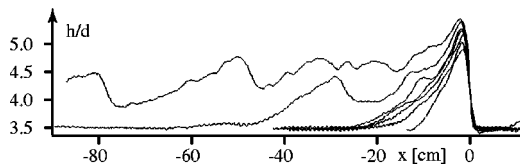
FIG. 9. Height profiles of moving fronts. All fronts were running from left to right at the same tilt angle 33°, and created about 60 cm above the measurement area with different initial mass. Small fronts have the shape of a shark fin, with monotonic rise and fall, and are stable. Fronts with a lot of moving mass spread in the direction of motion and disintegrate into several fronts of lesser height which eventually separate into stable fronts.

The fluctuations of the velocity at one angle, and the increase at low angles can be related to the variations of the moving height. If the velocity is plotted directly as a function of the moving height, a simple, roughly linear dependence is observed (inset of Fig. 10). It shows that the slope is not the essential parameter, and that as a first approximation the front velocity is given only by the moving height.

The increase of the velocity with height leads to the breaking of waves and/or the formation of shocks. Such shocks are visible in Fig. 9 at the front of the moving strip. The rear portion, on the other hand, would naturally spread, if the proportionality of the velocity with height was applied to each location in the wave. This is what occurs for large initial mass. But then it is surprising that a lonely wave can keep the same extension during its propagation. This shows that there is a typical length on which the flow is correlated, this length being the length of a typical lonely wave. To understand this, note that the continuously decreasing amplitude at the back of the lonely waves indicates that the wave is nowhere at an equilibrium for a homogeneous layer, otherwise a plateau would be observed. The shark fin shape therefore seems governed by the gradual trapping of the rolling grains at the back of the shock into a new static layer.
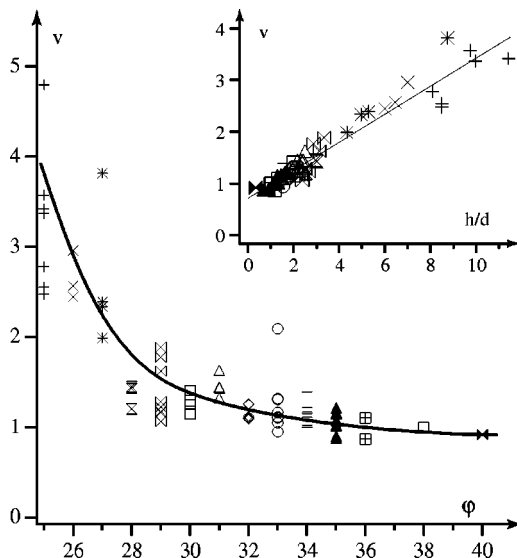

FIG. 10. Velocity of a moving front, in units of $\sqrt{gd} = 4.9$ cm/s. Main graph: Velocity as a function of the plane inclination φ. Inset: Velocity as a function of the relative height. The linear regression through the points (solid line) has a slope of 0.27 ± 0.1.
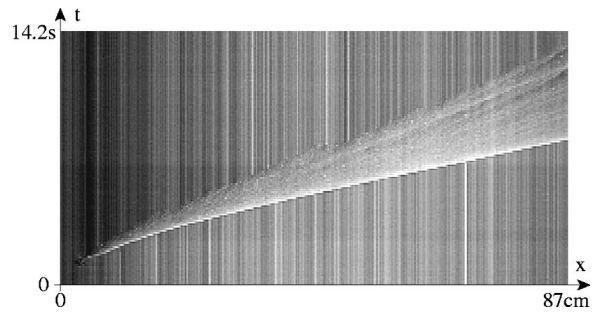

FIG. 11. Spatiotemporal representation of a triangular avalanche. The image (and Figs. 15, 16, and 22) was generated by isolating the section along the symmetry axis of an avalanche (in the direction of steepest slope) in each frame of a film, and juxtaposing the lines in the order of increasing time. Immobile particles appear at the same position from one frame to the next, and result in vertical striations in the spatiotemporal diagram. The tip of the avalanche (white, lower boundary) first accelerates and then reaches a constant velocity. The rear front is slower and rougher: Moving grains stop in packets or dissociate from the avalanche to go down as separate lonely wave (see also Figs. 12 and 15).

This corresponds to the measured surface velocity, decreasing quickly after the front like the height profile. Profiles of rock avalanches in chutes show similar profiles.[15]

IV. FLOW WITH AMPLIFICATION

Now the plane with the layer of thickness $h(\varphi)$ is tilted to a higher angle $\varphi + \delta\varphi$, in the metastable region. Consequently a perturbation gains mass on its way down, because the height of the layer in its tracks is $h(\varphi + \delta\varphi)$. Fig. 11 shows the evolution, in a spatiotemporal representation, of a triangular avalanche on a section along its symmetry axis. The origin of the avalanche is near the bottom-left. As the avalanche runs down to the right, it clearly spreads in the direction of motion.

One can distinguish two stages: At first, both head and rear fronts of the avalanche accelerate, and the avalanche tip becomes thicker. After a while, the fronts reach different limit velocities, and the height also saturates. The longitudinal extension of the avalanche finally increases linearly with time. This is because the mass gained (linearly) from running down over the prepared layer does not make the height increase any more, but spreads behind the tip. The rear of the flowing layer is unstable, and separates as lonely waves corresponding to this new inclination angle (Figs. 12 and 15).

A. Dynamical equilibrium

As in the case without amplification, the tip is the highest part of the flow (brightest in the images). It also has a very steep rise at the front, and a concave decrease to the flowing layer height behind. From Fig. 12 it can be seen that this head front remains invariant in form while the rear of the avalanche spreads.

The limit heights of avalanches are plotted in Fig. 13. The amplitude starts from the lonely wave amplitude, and then increases linearly with $\delta\varphi$ as the front velocity. But as it reaches two times the initial depth, it seems to saturate. This could mean that the flowing layer reaches the plane.
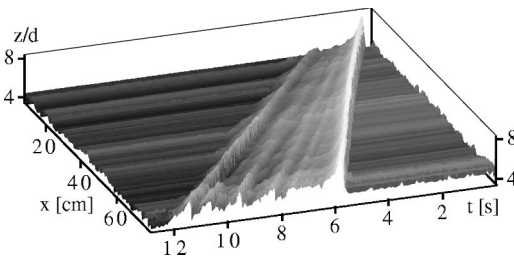
FIG. 12. Three-dimensional spatiotemporal representation of a triangular avalanche ($\varphi = 30°$, $\delta\varphi = 1°$). The local height (z axis, in bead diameters, and gray values) is measured along a line (x axis) and plotted as a function of time (t axis). The avalanche has been triggered beyond the far end, and grows in extension as it propagates. When it enters the visible region, the avalanche has already traveled ~ 2.5 relaxation lengths of 18 cm (see the text), and by midway through the tip has completely converged to the terminal velocity and height. The graph is viewed along this head front, which does not evolve any more: excess mass spreads to the rear instead, where the layer becomes unstable and breaks up into lonely waves.

B. Head front transient

To investigate the initial acceleration phase more closely, the position of the tip is plotted as a function of time in Fig. 14. It shows that the avalanche relaxes exponentially to the constant velocity regime. The characteristic time of the relaxation, 0.8 s in Fig. 14, is much greater than the typical internal relaxation time $\sqrt{d/g} = 5$ ms, and even the relaxation time based on the height of the moving front: $\sqrt{h/g} \simeq 10$ ms. This relaxation is as the shark fin shape rather due to the competition between the gain of the mass at the avalanche front and its spreading at the rear part. Measurements of this relaxation for different additional tilt to the same preparation angle $\varphi = 30°$ show that it corresponds in fact to a nearly constant length of stabilization: Independently of the final front velocity and height, it relaxes to the stable shape and velocity with the same characteristic distance 18 cm (~ 750 bead diameters).

This slow adaptation of the front velocity can also be observed for too high an initial velocity: In an experiment a layer was prepared such that it had a thickness of $h(\varphi)$ in the upper half of the plane, and of $h(\varphi + \delta\varphi)$ in the lower half,

FIG. 14. Position of the avalanche tip, as seen in a Galilean reference frame moving along at a velocity of 3.27 in nondimensional units (as in Fig. 18). The relaxation to constant velocity is well fitted by an exponential of characteristic time 0.8 s $= 160\sqrt{d/g}$.

with a step perpendicular to the direction of steepest slope in between. An avalanche was triggered at an inclination of $\varphi + \delta\varphi$ near the top of the plane. Evolving first on a thick layer, the avalanche grows in the expected triangular shape. The spreading in the direction of movement can be seen on the left-hand side of Fig. 15. On the lower half of the plane, however, the avalanche neither amplifies nor shrinks, because the layer thickness corresponds to the dynamical height at that angle. What we observe is that it tends to a lower limit velocity and tip height (the right-hand side of Fig. 15).

C. Uphill propagation

The dynamics of the avalanche tip shows the same acceleration and saturation for an uphill-propagating avalanche (see Fig. 16). Behind it however, the layer remains in motion
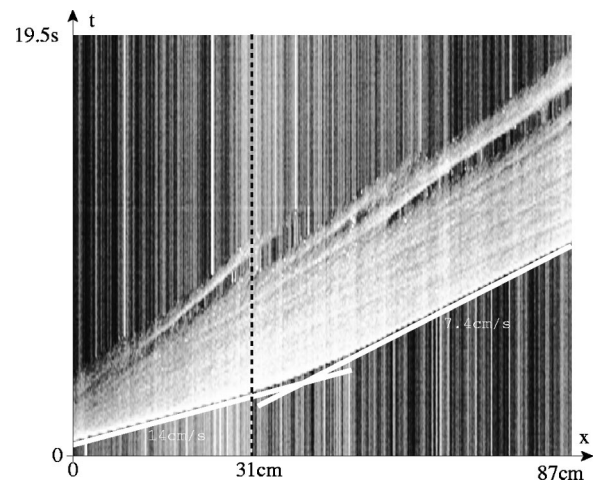
FIG. 15. Passage of an avalanche from an amplified region to a neutral one. The height of the layer is $h(\varphi)$ in the upper part of the plane ($x < 31$ cm) and $h(\varphi + \delta\varphi)$ in the lower part ($\varphi = 30°$, $\delta\varphi = 1°$). The avalanche is triggered at an inclination of $\varphi + \delta\varphi$, so that it is triangular and amplified for $x < 31$ cm, but does not grow anymore on the rest of the plane. The origin lies outside the spatiotemporal diagram to the left. After entering the neutral region at $x = 31$ cm, the front spreads, decreases in height, and slows down. This takes a considerable time and distance in terms of $\sqrt{d/g}$ and d. Note that both in the amplified and neutral regions waves at the rear dissociate from the main flow and drop back.
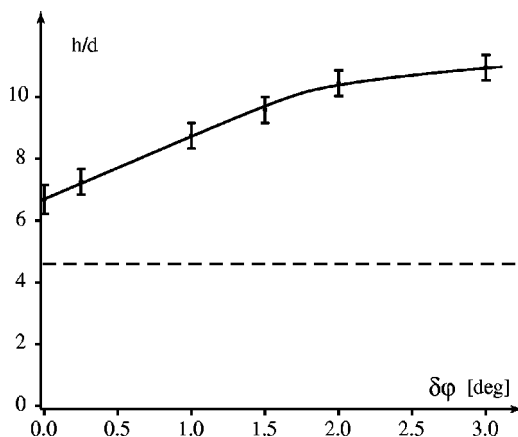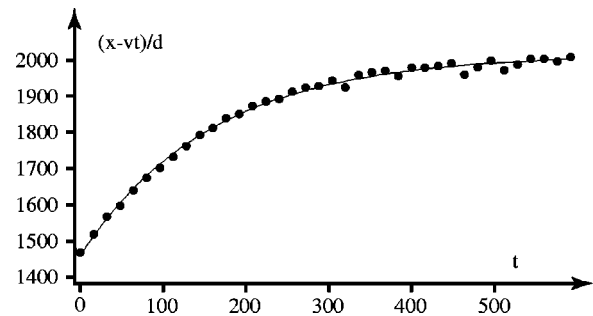

FIG. 13. Limit height of avalanches as a function of the additional tilt $\delta\varphi$ at which they were triggered. The height of the avalanche fronts increases to roughly twice the static layer thickness in front of the avalanche [dashed line at $h = (4.6 \pm 0.5)d$] and then seems to saturate.
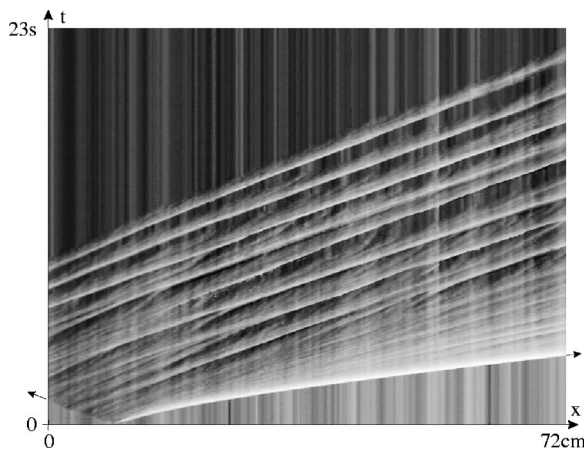
FIG. 16. Spatiotemporal representation of an uphill propagating avalanche. The tip of the avalanche (white, near the bottom) moves down to the right, while simultaneously a front moves uphill. Once the latter has reached the top of the plane (outside the image to the left), a slower rear stopping front runs down. Throughout the flowing part ripples are visible on the surface, separating into distinct moving packets which interact in various ways (cross, coalesce, etc.).

FIG. 17. Superposition of 100 boundaries of an uphill propagating avalanche ($\varphi = 30°, \delta\varphi = 2°$), scaled down around its origin by the time since triggering [Eq. (2), in units of $\sqrt{gd}$]. The real size of the avalanche varies by a factor 20, and the time between consecutive boundaries is 0.04 s. The lozenge represents the measured final speed of the tip, and the dashed lines represent the limit shape of the tip.

and its moving height is now determined by the mass flux depending on the velocity at which the instability front propagates uphill.

The top of Fig. 16 shows the end of the flow after the avalanches has reached the top of the plane, making the entire layer flow. Here it can be seen that the whole layer produced by the upward propagating front is unstable and decomposes into lonely waves, which can be seen to interact. This layer is thinner than the layer just behind the head front, as can be seen by considering the mass conservation. The instability is thus stronger, the thinner the layer is. This instability looks similar to hydrodynamic roll wave instabilities, which, however, occur at high Froude numbers.

In Fig. 17, 100 outlines of an uphill propagating avalanche have been scaled down by the time t elapsed since the beginning of the avalanche:

$$\widetilde{\mathbf{r}} = (\mathbf{r} - \mathbf{r_0})/t, \tag{2}$$

where $\mathbf{r_0}$ is the origin of the avalanche, $\mathbf{r} = (x,y)$ is any point on the boundary and $\widetilde{\mathbf{r}} = (\widetilde{x}, \widetilde{y})$ the resulting point on the rescaled outline. There are no free parameters. The rescaled boundaries collapse everywhere except at the tip of the avalanche. The rear and lateral front velocities are therefore constant from the beginning of the avalanche, contrary to the head velocity. This means that the mechanism responsible for the uphill and lateral propagation is immediately at the equilibrium, and that consequently the upper part of the avalanche is self-similar in time (the exponent being trivially 1). The stabilization of the upward and lateral front velocities from the very beginning may come from the fact that the mass put into motion is just advected away from these fronts, and thus does not influence the motion of the fronts themselves. By contrast, the head front is moving with the moving mass, which governs the velocity. It thus has to adjust and find an equilibrium.
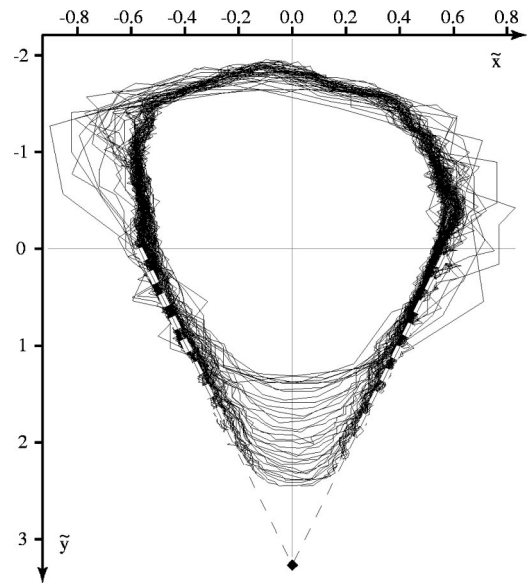
The tip of the avalanche does not scale as well as the rest of the boundary in Fig. 17. This comes first from the fact that as opposed to the other velocities, the head velocity presents a transient, first accelerating to reach its final constant value. The average velocity calculated previously therefore always underestimates the true velocity (whence the slow convergence in Fig. 17). Second, as was already stated, the head front is material, in the sense that it is advected along with the front and does not dilate. This can be seen from Fig. 18, where the outline of the tip is plotted in a reference frame advected at the terminal velocity of the tip (no scaling is performed). After a short transient, which corresponds to the acceleration phase, the curvature of the shape of the tip does not change any more and the outlines collapse.
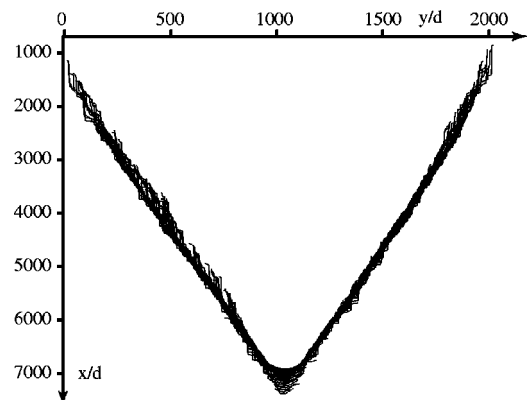

FIG. 18. Evolution of the tip of an avalanche. The tip of the avalanche at $\varphi = 30°, \delta\varphi = 2°$ (Fig. 17), as seen in a Galilean reference frame moving along at its terminal speed. The fronts collapse except around the apex, which accelerates and becomes blunt.
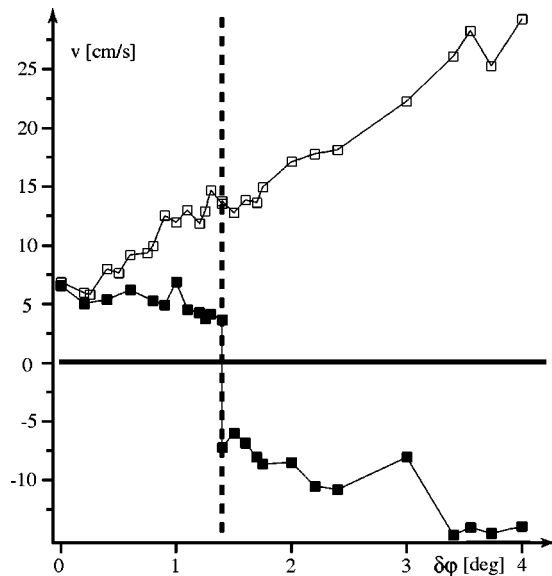
FIG. 19. Velocity of the avalanche tip and rear fronts. Measurements at the same angle $\delta\varphi$ have been averaged into a single point. Positive speeds are downhill. The terminal speed of the tip (open squares) increases approximately linearly with the additional tilt $\delta\varphi$ to the preparation angle $\varphi = 30°$. The rear of the avalanche (closed squares) has a constant speed of roughly $\sqrt{gd} = 4.9$ cm/s (dimensional estimation for the velocity of single grains) up to the transition for uphill propagation (vertical dashed line) where it abruptly reverses its sign. Above it, the absolute value of the speed increases with $\delta\varphi$.
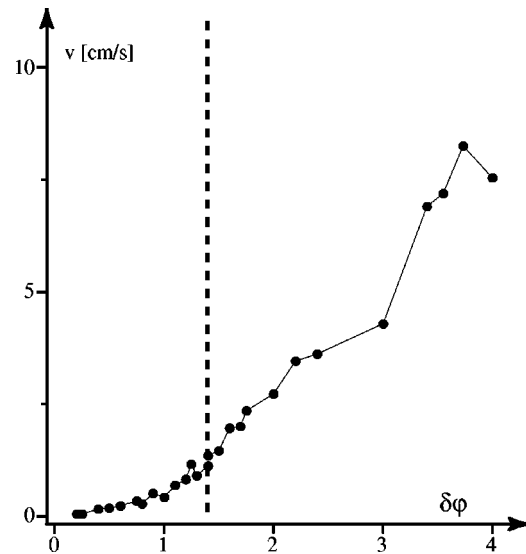

FIG. 20. Lateral velocity of avalanches. Measurements represent the mean of the right- and left-ward growth speed, and have been averaged over all avalanches at a same angle $\delta\varphi$. The speed increases quicker in the uphill propagating regime (right of the dashed line) than below.

D. Front velocities

In Fig. 19 we plotted the velocities of the avalanche fronts (head and rear) as a function of the additional tilt $\delta\varphi$ with respect to the preparation angle φ. At the preparation angle φ itself (that is for $\delta\varphi = 0$), we recover the nonvanishing downhill velocity of the nonamplifying solitary wave investigated in the previous section. The downhill velocity then increases very rapidly with $\delta\varphi$.

The velocity of the rear front is equal to the head velocity for $\delta\varphi = 0$ (lonely wave). It remains approximately constant up to the transition to upward motion (at $\delta\varphi = 1.4°$), where it changes sign to an opposite upward velocity. The measurements show that this transition is sharp. Above it, the upward rear velocity increases perceptibly (in absolute value).

The lateral velocity is plotted in Fig. 20. As the rear front, it is constant from the very beginning of the avalanche. It shows a larger increase above the threshold for uphill propagation. As opposed to the tip, the lateral extrema of the avalanche do notice the transition to the regime of uphill

propagation, in which the lateral propagation of the avalanche is much more efficient (the points of maximum lateral velocity are slightly uphill with respect to the origin in Fig. 21).
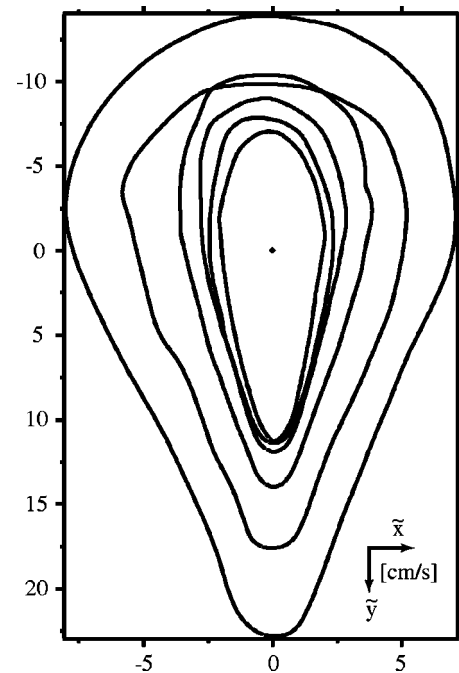
For triangular avalanches, we can also rescale the boundaries in the described way, but the collapse tells us nothing new. Indeed, the tip has the same shape and evolution as in the uphill propagating case, and the collapse of the triangular track is not a surprise if the apex of the triangle is chosen as scaling origin.

FIG. 21. Shapes of the uphill propagating avalanches with layer preparation angle $\varphi = 30°$ at additional tilt $\delta\varphi = 1.6°$, 1.75°, 2°, 2.4°, 3°, and 4°, respectively (from smallest to biggest). The tip is blunt because it is still partially in a transient: The longer one waits, the more the tip tends to the shape of a triangle (cf. Fig. 17). The aspect ratio of the upper part changes (the avalanche propagates uphill and practically not laterally at the triangular/uphill transition, and grows more and more isotropically as the angle increases) and the tip becomes concave for great $\delta\varphi$.
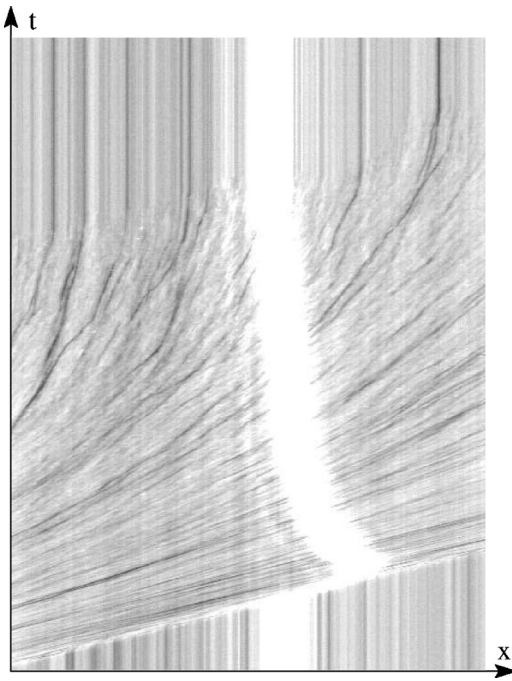
FIG. 22. Spatiotemporal representation of a triangular avalanche using a mixture of black and white colored beads ($100–200$ μm). As in Fig. 11, the front runs down from left to right, and vertical striations indicate motionless grains. The bright vertical line is created by a light sheet: Its displacement to the right is proportional to the local height. The particle traces show that the surface grains at the front have the same velocity as the front itself. Particles dropping back to the rear of the avalanche slow down quickly and get trapped into the new stable layer.

E. Material velocity

We also determined the material velocity of the surface particles by means of the particle image velocimetry (PIV) technique. Some tuning was necessary to apply this technique, originally used in hydrodynamics, to our case. In particular, we had to use a mixture of black and white glass beads (approximately 0.3% of black beads) and make the lighting more homogeneous to eliminate all shadows. The best spatial definition was obtained on sequences filmed by a high speed camera (500 frames per second). Figure 22 shows a spatiotemporal diagram of a triangular avalanche (compare to Fig. 11) constructed from such a sequence. The image confirms the visual observations on the other cases. The particles have the same velocity as the head front near that front itself, and slow down very fast toward the back. The bright line from the light sheet shows the characteristic shark fin shape of the height profile.

As can be seen from Fig. 23, the height and velocity profiles are strongly correlated. The local surface velocity seems to be simply proportional to the local height relative to the new static layer left behind the avalanche. It is tempting to interpret the deviation near the front shock as the region where the old static layer is still felt (on some kind of mobilization length) and where the relevant relative height should be measured with respect to the old layer. Here again, the front (group) velocity is equal to the surface (material) velocity to within 10%.
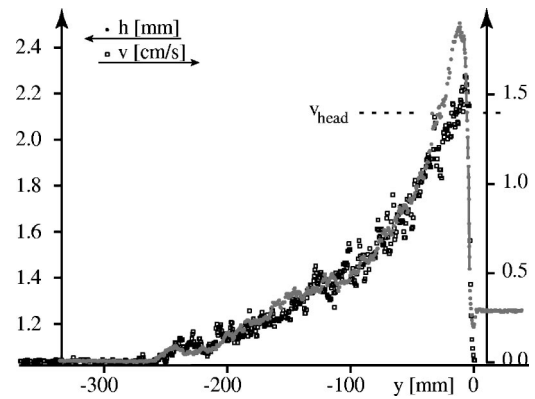

FIG. 23. Measurement of height and surface velocity profiles of a triangular avalanche. The simultaneous profiles in the direction of motion show that the velocity is everywhere proportional to the local height relative to the new static layer thickness (or to the old static layer thickness near the front). The maximum surface velocity corresponds to the group velocity of the head front, as can also be seen in Fig. 22.

V. DISCUSSION

We observe two types of avalanches in a metastable layer on a rough bed. For thin layers and inclinations close to the dynamical angle, the perturbation propagates only downhill and laterally, leaving behind a triangular track (Fig. 3). For thick layers and higher inclinations, the perturbation also propagates uphill, and eventually starts the whole layer moving (Fig. 4).

The main result is that in both cases the growth of the avalanche reaches a dynamical equilibrium. All fronts then propagate at constant speed, so that the area and the moving mass increase as the square of time. The rear front (in uphill propagating avalanches) in particular has a self-similar growth, whose shape (Fig. 21) remains to be explained. The amplitude of the head front is also observed to saturate.

In order to understand why the avalanche tip reaches a limit speed, recall the two main results on nonamplified, or ''lonely,'' waves (Sec. III): Their speed is governed essentially by their relative height, and they are only stable when their height is equal to a certain fraction of the thickness of the static layer. This means that an avalanche whose height is limited also has a limit speed. We argue that the height is indeed limited by the presence of the bottom. The ratio of the surface velocity (at the front) and the front velocity gives an idea of the depth of the flow. In a flow without mobilization for instance, like a flow on the rough plane without previous static layer, the surface velocity is much greater than the front velocity (because of mass conservation). It resembles the motion of a caterpillar, with all the material at the tip coming from the injection uphill. Section IV E showed that in our case, the surface velocity, and *a fortiori* any material velocity within the avalanche, is at most equal to the front velocity. The avalanche head therefore constantly mobilizes new grains and looses matter which drops back.[16] To estimate the depth of the flow, we have to make a hypothesis on the velocity profile across the layer. If we assume a linear velocity profile (as suggested by experiments[17,18]), the thickness of the moving layer must be twice its relative height with respect to the static layer.[19] In other words, the static/
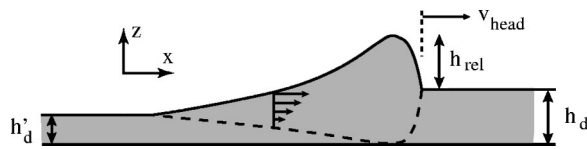
FIG. 24. Possible view of an avalanche cross section. Supposing a linear velocity profile, we conclude from the measurements that the avalanche mobilizes the static layer to a depth which corresponds roughly to its relative height above the static layer thickness.

flowing interface is roughly symmetric to the free surface profile (Fig. 24). It would therefore be natural that the nature of the flow changes when the total height of the front exceeds two times the static layer depth, so that it reaches the static plane. We saw indeed that the height of avalanches seems to grow more slowly (or to saturate) above this value (Fig. 13). The further increase of the avalanche velocity at larger inclination (Fig. 19) indicates an increase of the velocity gradient, as observed for a flow on a rough bottom.[6] For a yet unknown reason, the mobilized mass then spreads toward the back instead of accumulating at the front.

A second remark concerns the profile of the avalanche. The head of the avalanche is a shock wave with a steep front, a maximum height and a monotonic decrease toward the flowing layer at the back. The same height profile is found in lonely waves (Fig. 9), which are pure mobilization-deposition waves without amplification. On the other hand, a maximum of the height at the head front is not observed in experiments without previous static layer.[20] The particular shark fin shape of the head front with a peak thus seems to be characteristic of a shock front with mobilization of material. The tip sets static material in motion at a certain velocity, and feeds it to the flowing layer behind, thereby determining the flowing layer thickness (as opposed to chute flow experiments,[6,20] where the mass flow rate is imposed at the injection). It is interesting to see how the simple local relation between height and velocity (Fig. 23), which could be read as a quasi-instantaneous equilibrium across the layer, creates globally a nonuniform, out-of-equilibrium shape by steepening the front and the flattening the rear. This shark fin shape of the head of the avalanche is then conserved in a dynamic equilibrium governed by mobilization and deposition (Fig. 12). It is not clear how the relaxation of this dynamic equilibrium (toward a state where the loss toward the back compensates the gain through mobilization) introduces a new, much longer time scale (Fig. 14).

A first problem that remains is to understand this particular shape of the head front, observed in amplified or non-amplified flows and also in debris flows experiments.[15] But the main problem is to explain the saturation in velocity and height, which is found to be directly related to the height of the static layer thickness. This leads to the question of what happens for very thick sand piles when inclined in the metastable interval (this is not the case of dunes, whose inclina-

tions can hardly be changed). If the presence of the bottom is the only limiting factor to the amplification of avalanches, then there should be no limit to the amplitude on very deep layers. Preliminary experiments show that the acceleration phase becomes longer with increasing depth. Further measurements need to be done to conclude whether there is no more saturation for thick piles, or whether the relaxation simply takes much longer. This could have some importance in fresh snow avalanches,[21] to explain that larger avalanches travel much farther than could be expected from comparison to small ones.

ACKNOWLEDGMENT

[1] D. A. Augenstein and R. Hogg, ''An experimental study of the flow of dry powders over inclined surfaces,'' Powder Technol. **19**, 205 (1978).

[2] O. Hungr and N. R. Morgenstern, ''Experiments on the flow behavior of granular materials at high velocity in an open channel,'' Geotechnique **34**, 405 (1984).

[3] J. W. Vallance, ''Experimental and field studies related to the behavior of granular mass flows and the characteristics of their deposits,'' Ph.D. thesis, Michigan Technological University, 1994.

[4] S. B. Savage and K. Hutter, ''The motion of a finite mass of granular material down a rough incline,'' J. Fluid Mech. **199**, 177 (1989).

[5] P. C. Johnson, P. Nott, and R. Jackson, ''Frictional-collisional equations of motion for particulate flows and their application to chutes,'' J. Fluid Mech. **210**, 501 (1990).

[6] E. Azanza, F. Chevoir, and P. Moucheront, ''Experimental study of collisional granular flows down an inclined plane,'' J. Fluid Mech. **400**, 199 (1999).

[7] O. Pouliquen, ''Scaling laws in granular flows down rough inclined planes,'' Phys. Fluids **11**, 542 (1999).

[8] A. Daerr, ''Dynamique des avalanches,'' Ph.D. thesis, University of Paris VII (France) URL: http://www.lps.ens.fr/recherche/formes/thesis.html, 2000.

[9] S. R. Nagel, ''Instabilities in a sandpile,'' Rev. Mod. Phys. **64**, 321 (1992).

[10] O. Pouliquen and N. Renaut, ''Onset of granular flows on an inclined rough surface: Dilatancy effects,'' J. Phys. II **6**, 923 (1996).

[11] A. Daerr and S. Douady, ''Two types of avalanche behavior in granular media,'' Nature (London) **399**, 241 (1999).

[12] O. Pouliquen, J. Delour, and S. B. Savage, ''Fingering in granular flows,'' Nature (London) **386**, 816 (1997).

[13] L. Quartier, B. Andreotti, S. Douady, and A. Daerr, ''Dynamics of a grain on a sandpile model,'' Phys. Rev. E **62**, 8299 (2000).

[14] L. Samson, I. Ippolito, D. Bideau, and G. G. Batrouni, ''Motion of grains down a bumpy surface,'' Chaos **9**, 639 (1999).

[15] T. Takahashi, *Debris Flow* (Balkema, Brookfield, VT, 1991).

[16] The fact that a given grain stays in the avalanche only for a finite time could explain why we do not see segregation phenomena in the avalanche.

[17] J. Rajchenbach, ''Granular flows,'' Adv. Phys. **49**, 229 (2000).

[18] S. Douady, B. Andreotti, and A. Daerr, ''On granular surface flow equations,'' Eur. Phys. J. B **11**, 131 (1999).

[19] This estimation of the flowing depth allows us to convert the slope of the velocity-height dependency in Fig. 10, whose value is $(0.27 \pm 0.1)\sqrt{g/d}$, into a typical velocity gradient inside the layer of 0.14, which is comparable to other measurements in chutes (Ref. 6) and rotating drums $[\approx 0.28$ (Ref. 17)].

[20] O. Pouliquen, ''On the shape of granular fronts down rough inclined planes,'' Phys. Fluids **11**, 1956 (1999).

[21] D. McClung, *Avalanche Handbook* (Mountaineers, Seattle, 1993).